



## Processability improvement and strength enhancement in laser powder bed fusion of AlMgZr and AlMgZr-Ti alloys

Mengzhen Zhu, Jianying Wang, Tao Wen, Zhongxue He, Xixi Dong, Dong Qiu, Shouxun Ji, Yun Wang & Hailin Yang

To cite this article: Mengzhen Zhu, Jianying Wang, Tao Wen, Zhongxue He, Xixi Dong, Dong Qiu, Shouxun Ji, Yun Wang & Hailin Yang (2025) Processability improvement and strength enhancement in laser powder bed fusion of AlMgZr and AlMgZr-Ti alloys, Virtual and Physical Prototyping, 20:1, e2523546, DOI: [10.1080/17452759.2025.2523546](https://doi.org/10.1080/17452759.2025.2523546)

To link to this article: <https://doi.org/10.1080/17452759.2025.2523546>



© 2025 The Author(s). Published by Informa UK Limited, trading as Taylor & Francis Group



Published online: 04 Jul 2025.



Submit your article to this journal [↗](#)



Article views: 233



View related articles [↗](#)



View Crossmark data [↗](#)

# Processability improvement and strength enhancement in laser powder bed fusion of AlMgZr and AlMgZr-Ti alloys

Mengzhen Zhu<sup>a</sup>, Jianying Wang<sup>a</sup>, Tao Wen<sup>a</sup>, Zhongxue He<sup>a</sup>, Xixi Dong<sup>b</sup>, Dong Qiu<sup>c</sup>, Shouxun Ji<sup>d</sup>, Yun Wang<sup>d</sup> and Hailin Yang<sup>a</sup>

<sup>a</sup>State Key Laboratory of Powder Metallurgy, Central South University, Changsha, People's Republic of China; <sup>b</sup>College of Mechanical and Electrical Engineering, Nanjing University of Aeronautics and Astronautics, Nanjing, People's Republic of China; <sup>c</sup>Centre for Additive Manufacturing, School of Engineering, RMIT University, Melbourne, Australia; <sup>d</sup>Brunel Centre for Advanced Solidification Technology (BCAST), Brunel University London, Uxbridge, UK

## ABSTRACT

The Al<sub>3</sub>(Ti, Zr) phase, which exhibits a lower formation enthalpy, was incorporated to improve the processability and strength of AlMgZr alloys fabricated by laser powder bed fusion (PBF-LB). The results confirmed that the crack-free AlMgZr-Ti alloy exhibited a relative density of 99.7% and a fine grain size of ~ 2.5 µm. The improved processability can be attributed to grain refinement and the columnar-to-equiaxed transition (CET), which is induced from promoted heterogeneous nucleation by *in-situ* Al<sub>3</sub>(Ti, Zr) phase and high grain growth restriction factor by segregation of Ti at the interface. During solidification, Al<sub>3</sub>Ti phase was precipitated initially and Zr was incorporated into the Al<sub>3</sub>Ti lattice in the subsequent precipitation, accelerating Zr precipitation from α-Al matrix. Through experimental results and calculations of formation enthalpy in combination, the Al<sub>3</sub>(Ti, Zr) phase was most likely to be Al<sub>3</sub>(Ti<sub>5/6</sub>, Zr<sub>1/6</sub>). Meanwhile, the AlMgZr-Ti alloy exhibited superior strength in comparison with the counterpart of AlMgZr alloy, where the enhancement of YS (408 MPa) and UTS (432 MPa) is 119% and 42.6%, respectively, with the UTS of the AlMgZr-Ti alloy maintaining 182 MPa at 300 °C.

## ARTICLE HISTORY

Received 3 March 2025

Accepted 17 June 2025



## KEYWORDS

Aluminium alloys; laser powder bed fusion; microstructure; strength enhancement; thermal stability

## 1. Introduction

Laser powder bed fusion (PBF-LB) has increasingly garnered attention in the industrial sector owing to the advantages of manufacturing complex geometries and operational flexibility [1-3]. Up to date, a number of aluminium (Al) alloys including AlSi10Mg, AlSi7Mg, AlSi12 and Scalmalloy are capable of being manufactured by PBF-LB. Among them, eutectic and near-eutectic alloys have excellent processability and high strength, primarily attributed to the presence of abundant eutectic microstructures and narrow range of solidification. Nevertheless, due to the highly volume fraction of eutectic phase, the alloys tend to have low ductility (<10%). The wrought alloys such as Al-Cu, Al-Mg, Al-Mg-Si and Al-Zn-Mg-Cu alloys can offer high strength, but have not yet been widely adopted in PBF-LB due to high hot cracking susceptibility [4]. It was reported that the additions of alloying elements (e.g. Sc/Zr/Ti) can facilitate nucleation and growth processes, leading to the columnar to equiaxed transition (CET) and hot cracking mitigation, thereby significantly enhancing processability and

mechanical properties [5-7]. Also, the addition of alloying elements could achieve a more uniform microstructure and is easily applied in industry [8,9]. Al-Mg based alloys were followed with interest as they offer high specific strength and good strong plasticity. Research has demonstrated that the PBF-LB processability of AA5083 alloy was significantly improved by the addition of Zr, in which heterogeneous nucleation of nanoscale L1<sub>2</sub>-Al<sub>3</sub>Zr phase was promoted, leading to refined grains and eliminated hot cracking during solidification [10]. It was revealed that AlMgZr alloy could be processed by PBF-LB to obtain samples with nearly 100% relative density [11]. The microstructural characteristics of the PBF-LB AlMgZr alloys are usually featured with fine grains interconnects at the melt pool boundaries and coarse columnar ones in the central region of the melt pool. These alloys have achieved a combination of high yield strength (YS) (~ 316 MPa), ultimate tensile strength (UTS) of 341 MPa and high tensile elongation (~ 20%) [12]. Meanwhile, Sc and Zr have also been simultaneously adopted in the Al-Mg alloys to boost the nucleation potential for fine

**CONTACT** Hailin Yang  y-hailin@csu.edu.cn  State Key Laboratory of Powder Metallurgy, Central South University, Changsha 410083, People's Republic of China

© 2025 The Author(s). Published by Informa UK Limited, trading as Taylor & Francis Group

This is an Open Access article distributed under the terms of the Creative Commons Attribution License (<http://creativecommons.org/licenses/by/4.0/>), which permits unrestricted use, distribution, and reproduction in any medium, provided the original work is properly cited. The terms on which this article has been published allow the posting of the Accepted Manuscript in a repository by the author(s) or with their consent.

equiaxed grains. Sc modifies the solidification sequence, giving rise to the formation of primary  $L_{12}\text{-Al}_3(\text{Sc, Zr})$  phases during solidification and secondary  $\text{Al}_3(\text{Sc, Zr})$  precipitates following ageing [13]. Although the grains were refined to some extent, a bimodal microstructure was still observed in the as built alloy [14]. The as-built Al-Mg-Sc-Zr alloy showed YS and UTS values of 280 and 350 MPa, and the strength improvement was mainly dependent on ageing treatment, with the YS and UTS reaching 460 and 485 MPa after ageing at 350 °C for 24 h [14].

Recently, creative combination of various commercial powders was carried out to produce crack-free PBF-LBed Al alloys with improved mechanical properties [15,16]. A straightforward and cost-efficient approach can be developed to produce crack-free components with enhanced mechanical properties for the commercialisation of high-strength Al alloys. Experimental evidence has demonstrated the efficacy of modifying AA7075 Al alloy with Ti-6Al-4 V ( $\text{TC}_4$ ) powders in eliminating hot cracks, thereby substantially refining the grains [15]. The incorporation of nucleation particles or high growth restriction factor solutes into Al alloys can facilitate CET or/and grain refinement during PBF-LB [17-19]. Similar to  $\text{TC}_4$  powders, Ti is considered one of the most effective grain-refining solutes in Al alloys, and it possesses a higher grain-restricting ability than Zr [20]. For instance, mechanically alloyed Al-25 at.% Ti particles have been introduced to an AA6061 Al alloy to promote the CET and hot cracking elimination [21]. The micro-sized Ti powders in Al-Mg alloy promote the CET and grain refinement [22]. Although the grain refinement and strength enhancement from *ex-situ* or *in-situ* elements addition are encouraging, there are few studies on the effect from the nucleation particles consisting of both *ex-situ* elements and *in-situ* elements.

The present study aims to reveal the effect of *ex-situ* Ti addition on an AlMgZr alloy, in which micron-sized Ti powders is mechanically mixed with AlMgZr alloy powders. Solidification behaviour and microstructural evolution during PBF-LB process are investigated systematically. Discussion is focused on grain refinement and CET, the processability improvement and strengthening mechanisms of the AlMgZr-Ti alloy.

## 2. Experimental procedures

### 2.1. Alloy powder

AlMgZr alloy powders with an average particle size of 31.5  $\mu\text{m}$  were produced using a vacuum induction gas atomisation process. The chemical composition was characterised using inductively coupled plasma atomic emission spectroscopy (ICP-AES). The analysed powder composition was determined to be 4.28 wt.% Mg and 0.73 wt.% Zr.

Commercial purity (CP) Ti powder, with a purity of at least 99% with an average particle size of 37.3  $\mu\text{m}$ , was mixed with the AlMgZr alloy powder at a concentration of 2 wt.% Ti. This mixing was performed in a V-type powder mixer for a duration of 12 h. SEM images in Figure 1(a, b) and EDS mapping in Figure 1(b<sub>1</sub>-b<sub>4</sub>) demonstrate that, after the mixing, Ti particles uniformly distributed among the AlMgZr particles with both powder particles being of spherical morphology. The size distributions of the AlMgZr and Ti powders is shown in Figure 1(c, d).

### 2.2. Laser powder bed fusion process

A 500 W fibre laser beam with a wavelength of 1064 nm was employed in this study. To reduce oxidation during the PBF-LB process, an argon gas flow was introduced. Cuboid specimens measuring  $10 \times 10 \times 10 \text{ mm}^3$  and  $80 \times 10 \times 10 \text{ mm}^3$  were produced on an AlSi10Mg substrate plate. Different scan speeds (600, 800, 1000, 1200 mm/s) were applied at 310 W. A powder bed thickness ( $t$ ) of 30  $\mu\text{m}$ , a hatch distance ( $h$ ) of 100  $\mu\text{m}$  were maintained, along with a bi-directional scanning approach the included a 67° rotation between the successive layers. The as-built AlMgZr and AlMgZr-Ti samples were shown in Figure 1(e, f). The optimal settings for laser power ( $P$ ) and scan speed ( $v$ ) were 310 W and 1000 mm/s. The bulk density was measured using the principle of Archimedes.

### 2.3. Microstructural characterisation

Samples for microstructural characterisation were prepared from the resultant AlMgZr-Ti alloy using the standard metallographic procedure. The microstructure was characterised with a TESCAN MIRA4 SEM using the back-scattered electrons (BSE). Electron backscatter diffraction (EBSD) scans were conducted over a  $200 \times 200 \mu\text{m}^2$  area with an accelerating voltage of 20 kV and a step size of 0.25  $\mu\text{m}$ . Transmission electron microscopy (TEM) specimens were prepared by first grinding the samples down to 50  $\mu\text{m}$ , and then performing precision ion beam milling. TEM were carried out using a Talos-F200X. X-ray diffraction (XRD) data for the as-built samples were collected using a DX-2700B X-ray diffractometer with Cu-K $\alpha$  radiation. The scans covered a  $2\theta$  range from 20° to 80°, employing a step size of 0.02° and a scanning speed of 2° per minute. The size of the precipitates was estimated using ImageJ software.

### 2.4. Mechanical property testing

Hardness was determined by a BUEHLER5104 Vikers device under 100 g load for 15 s holding time, with an

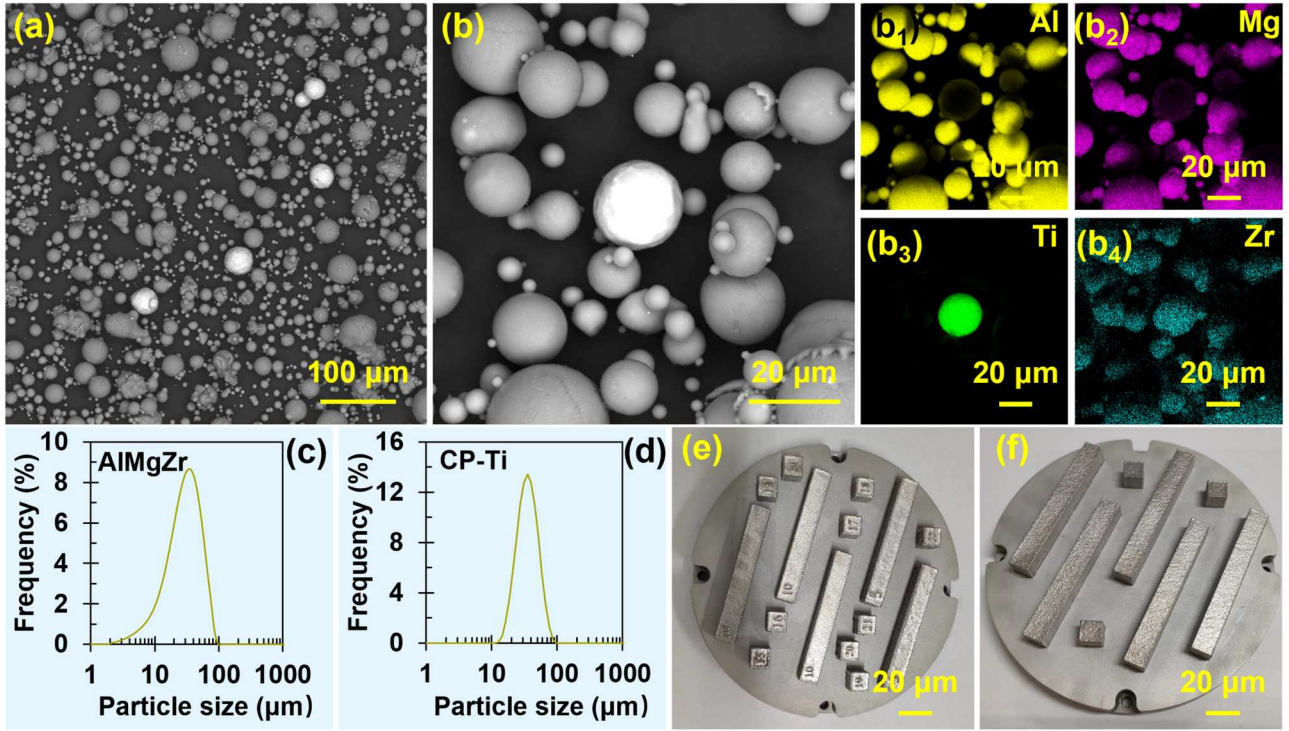


**Figure 1.** (a, b) BSE images of AIMgZr-Ti alloy powder mixture showing (a) the morphology of Ti particles and (b) the higher magnification of Ti particles and EDS elemental mapping for Al, Mg, Zr, and Ti (b<sub>1</sub>-b<sub>4</sub>); (c, d) particle size distribution of (c) AIMgZr powder and (d) Ti powder, and the as-built (e) AIMgZr and (f) AIMgZr-Ti samples.

average of 5 points was taken as the final result. Rectangular tensile test specimens were prepared from samples with a gauge length of 20 mm, width of 4 mm, and thickness of 2 mm. These specimens were mechanically cut to ensure the loading direction was oriented perpendicular to the building direction. Tensile tests were conducted in accordance with the ASTM E8 standard using an Instron-3369 universal testing machine. The tests were performed at room temperature (25 °C) with a cross-head speed of 1 mm/min. Strain was measured using a 12.5 mm extensometer. Tensile tests at 300 °C were conducted using a WDW-100C testing machine. All tensile specimens were tested at least five samples and the average was taken as the data used in this paper.

## 2.5. Ab initio calculations

To investigate the relative stability of the L1<sub>2</sub> structure for the Al<sub>3</sub>Ti, Al<sub>3</sub>Zr, and Al<sub>3</sub>(Ti, Zr) compounds, the total energies ( $E_t$ ) and formation enthalpy ( $\Delta H_f$ ) were calculated by computational simulations. For the total energy calculations of these compounds with L1<sub>2</sub> structure (four atoms in the primitive cell), a 3 × 2 × 1 supercell was determined to be appropriate. Density functional theory (DFT) calculations were performed using the Vienna Ab initio Simulation Package (VASP) with

the Perdew–Burke–Ernzerhof (PBE) exchange–correlation functional within the generalised gradient approximation (GGA) [23]. A plane-wave basis set with an energy cutoff of 350 eV was employed, and a 5 × 7 × 3 k-point gamma-centered sampling was used. The minimisation process for each displaced configuration terminated when the ionic force on each atom was reduced to below 0.01 eV/Å. The calculated total energies of Al fcc, Zr hcp, and Ti hcp are – 4.1967 eV/atom, – 7.7617 eV/atom and – 8.5192 eV/atom, respectively. The formation enthalpy was determined using the following Equation [24]:

$$\Delta H_f^{Al_{n_1}Ti_{n_2}Zr_{n_3}} = \frac{E_t^{Al_{n_1}Ti_{n_2}Zr_{n_3}} - n_1 E_t^{Al} - n_2 E_t^{Ti} - n_3 E_t^{Zr}}{n_1 + n_2 + n_3} \quad (1)$$

where  $n_1$ ,  $n_2$  and  $n_3$  represent the number of Al, Ti and Zr atoms in the unit cell.  $E_t^{Al_{n_1}Ti_{n_2}Zr_{n_3}}$ ,  $E_t^{Al}$ ,  $E_t^{Ti}$ ,  $E_t^{Zr}$  denote the total energies of the compound  $Al_{n_1}Ti_{n_2}Zr_{n_3}$ , and pure Al, Ti and Zr, respectively.

## 3. Results

### 3.1. Processability improvement

The optical microscopy (OM) images in Figure 2 show the general microstructure of AIMgZr and AIMgZr-Ti alloys, with the corresponding volumetric laser energy



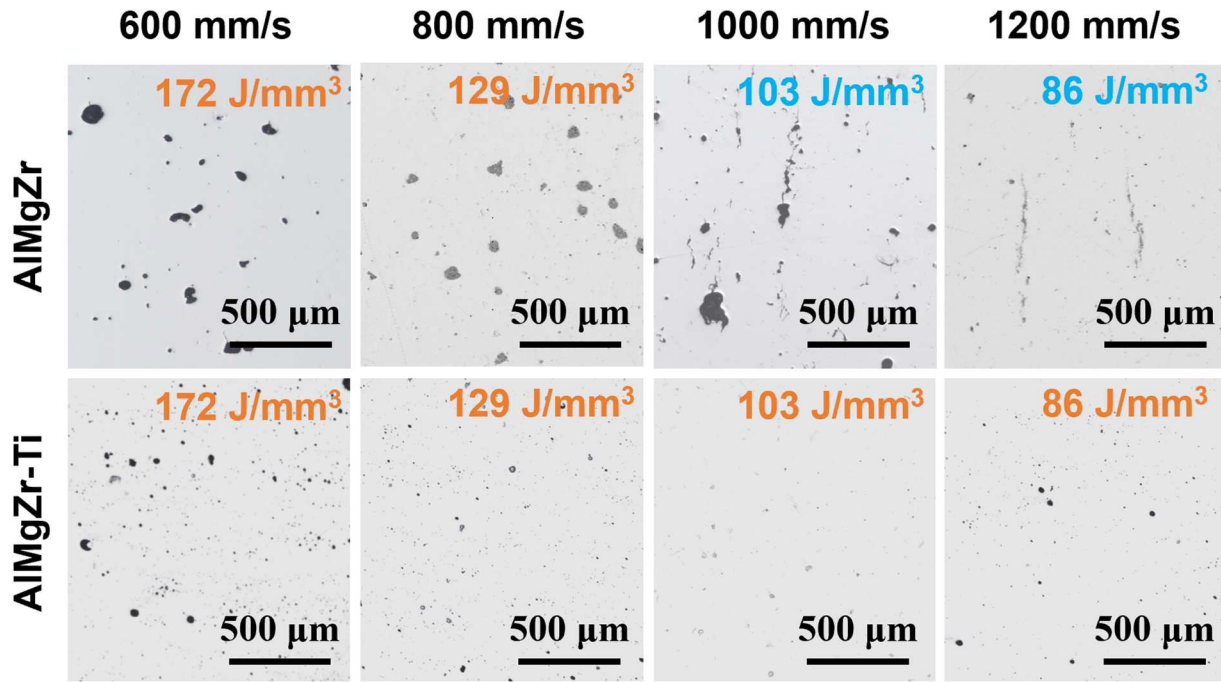


**Figure 2.** Optical microscopy images showing the general microstructure of AlMgZr and AlMgZr-Ti samples along the building direction at a fixed laser power at 310 W.

density ( $VED$ ) indicated. The  $VED$  is calculated using the formula  $VED = P/vht$  [25]. Obvious pore defects are found in the AlMgZr specimens fabricated with both high and low  $VED$ s, a finding that aligns with previous research [26]. When the laser power was 310 W, macroscopically crack-free AlMgZr alloy featured with a trace of pores was successfully produced within the limited laser scanning speed of  $v = 600\text{--}800$  mm/s. When  $v$  increased from 800 mm/s to 1000 mm/s, microcracks were found. With increasing scanning speed to higher than 1000 mm/s, macroscopic cracks were seen to propagate paralleled to the building direction. The microstructural characteristics indicate that the densification behaviour of the PBF-LBed samples was strongly dependent on the energy input [27]. In contrast, AlMgZr-Ti alloy exhibits crack-free, indicating that the Ti-containing alloy is highly crack resistant. With a wide processing window of  $86\text{--}172$  J/mm<sup>3</sup>, a relative density as high as 99.7% was achieved at  $103$  J/mm<sup>3</sup> for the Ti-modified AlMgZr alloy.

### 3.2. Microstructural characterisation

Figure 3 compares the macrostructures of both alloys on the cross-sections. The crack-prone and crack-free areas in the AlMgZr alloy were shown in Figure 3(a) and (b). The cracks primarily propagated along the boundaries of these columnar grain, consistent with prior research

on the cracking behaviour of other PBF-LB processed Al alloys that exhibit crack susceptibility [28,29]. The average grain size in crack-prone regions was  $\sim 10.5$   $\mu\text{m}$ , as seen in Figure 3(d). The areas surrounding the cracks were predominantly characterised by a coarse columnar microstructure, with the columnar grain varying in size from a few microns up to  $26.0$   $\mu\text{m}$ . Figure 3(g) reveals that these columnar grains possess a pronounced  $\langle 001 \rangle$  texture. In contrast, the crack-free region of the AlMgZr alloy, illustrated in Figure 3(b, e), demonstrated a notable decrease in the area occupied by coarse columnar grains, with an average grain size of  $7.2$   $\mu\text{m}$ . Accordingly, there was an increase in the proportion of randomly oriented equiaxed grains, and the  $\langle 001 \rangle$  texture was weakened (Figure 3(h)). Interestingly, the introduction of Ti into the AlMgZr alloy resulted in evident grain refinement, producing a fully equiaxed and fine grain structure as small as  $\sim 2.5$   $\mu\text{m}$  (Figure 3(c, f)). From Figure 3(i), the pole value is further reduced as the alloy is completely equiaxial. the KAM maps depicted in Figure 3(j–l) demonstrate that the misorientation values ( $0.65^\circ$ ) was significantly reduced with the introducing of a high proportion equiaxed grains in the AlMgZr-Ti samples.

The XRD results in Figure 4(a–c) demonstrate that the AlMgZr alloy consisted of  $\alpha\text{-Al}$  and  $\text{Al}_3\text{Zr}$  phase, and a trace of  $\text{Al}_3(\text{Ti}, \text{Zr})$  phase was visible in the AlMgZr-Ti alloy. As the Zr element, with a larger

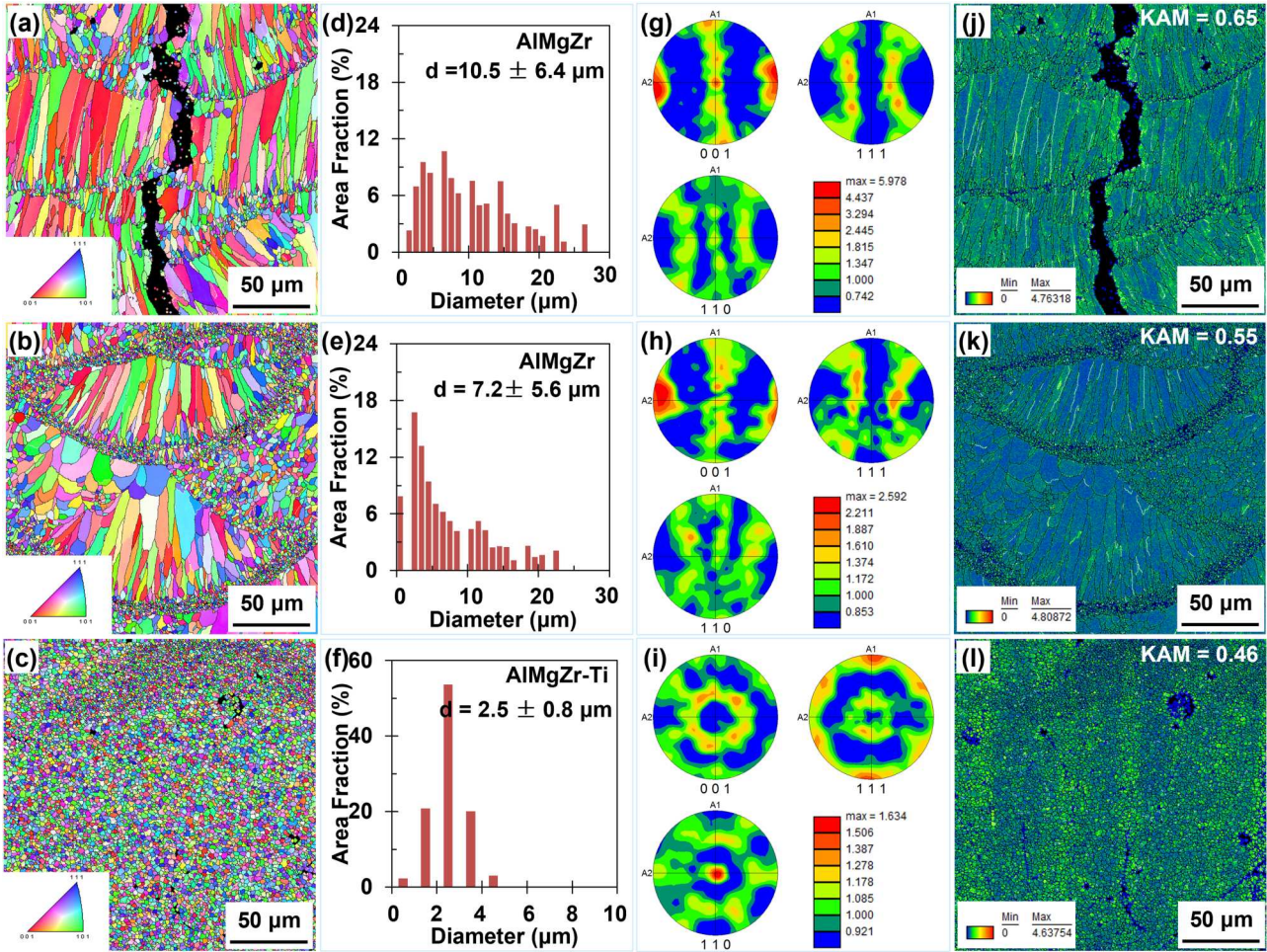


**Figure 3.** (a–c) EBSD maps, (d–f) grain size distribution, (g–i) pole figures and (j–l) KAM maps are presented for: (a, d, g, j) crack-prone areas in the AlMgZr alloy, (b, e, h, k) crack-free areas in the AlMgZr alloy, and (c, f, i, l) the AlMgZr-Ti samples.

atomic size, replaced Ti in the  $\text{Al}_3\text{Ti}$  phase, the  $\text{Al}_3(\text{Ti}, \text{Zr})$  phase synthesised in the AlMgZr-Ti alloy exhibits a peak shift toward lower angle with relative to the characteristic diffraction peak position of  $\text{Al}_3\text{Ti}$ . Similar phenomena have been reported in prior literature

[30]. In addition, the  $\langle 001 \rangle$  texture was disappeared as CET occurred.

In Figure 5(a, b), the microstructure of the AlMgZr alloy consisted of the primary dendritic  $\alpha\text{-Al}$  grains and  $\text{Al}_3\text{Zr}$  phase. The average size of  $\text{Al}_3\text{Zr}$  precipitates

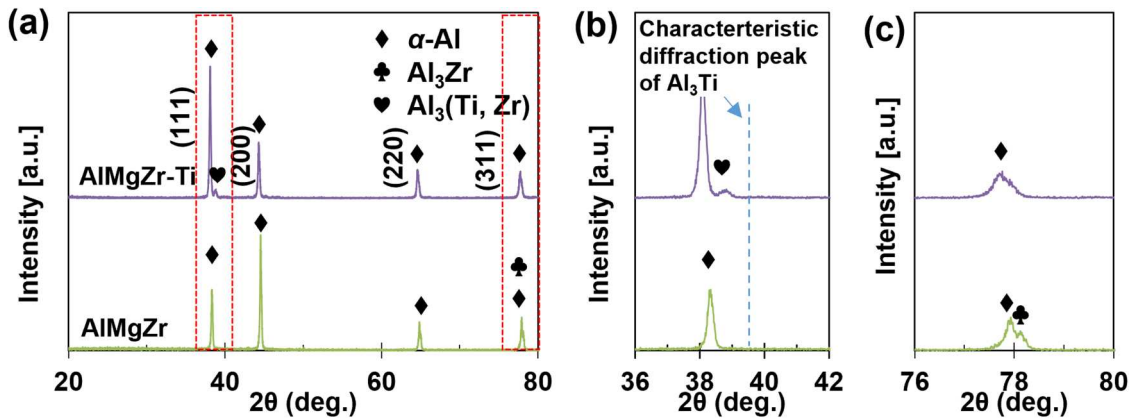


**Figure 4.** (a) XRD pattern of the AlMgZr and the AlMgZr-Ti alloys; (b, c) the enlarged view of the red box selected area in (a).



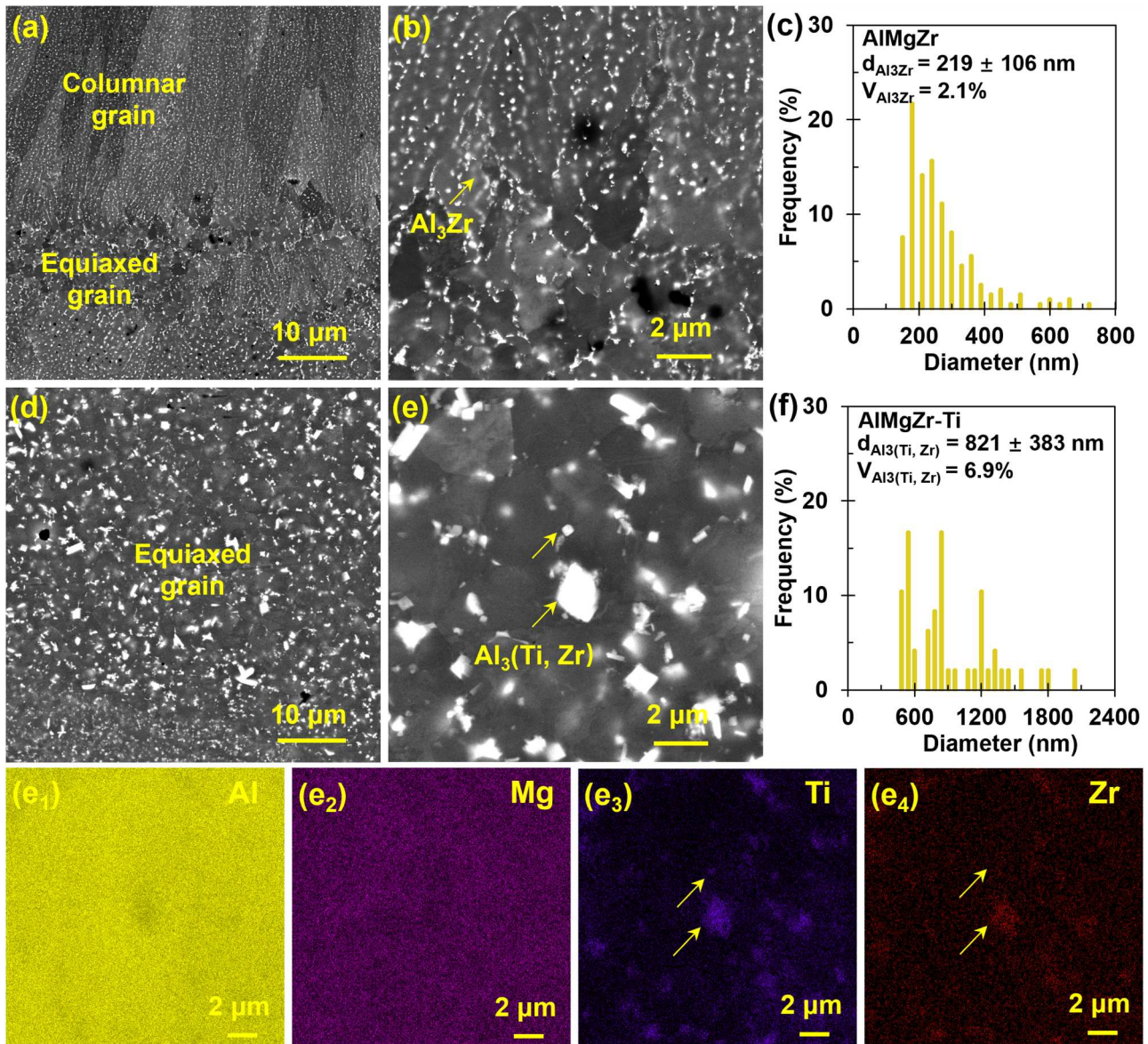


**Figure 5.** SEM images and precipitates size distribution of (a–c) the AlMgZr alloy and (d–f) the AlMgZr-Ti alloy, EDS maps in (e<sub>1</sub>–e<sub>4</sub>) highlight the distribution of Al, Mg, Zr and Ti, indicating the formation of Al<sub>3</sub>(Ti, Zr) phase.

was 219 nm, and the volume fraction was 2.1%, as shown in Figure 5(c). Meanwhile, the equiaxed grains predominantly observed along melt pool boundaries and coarse columnar grains were distributed at the melt pool centre that extended radially from the edge of the melt pool towards the centre. Comparatively, Ti-induced grain refinement in the AlMgZr alloys was evidently resulted from the formation of Al<sub>3</sub>(Ti, Zr) phase in Figure 5(d, e). Moreover, remarkable changes in the size and volume fraction of Al<sub>3</sub>(Ti, Zr) precipitates have been observed. The average size of Al<sub>3</sub>(Ti, Zr) precipitates was 821 nm, the volume fraction increased to 6.9% (Figure 5(f)). Furthermore, the homogeneously cubic intermetallic phase distributing among the fine equiaxed grains of AlMgZr-Ti alloy

were enriched in Al, Ti and Zr, as indicated in Figure 5(e<sub>1</sub>–e<sub>4</sub>).

Equiaxed grains and columnar grains (see Figure 6(a–c)) were obtained in the AlMgZr alloy due to an irregular aggregation distribution of Al<sub>3</sub>Zr phases that act as the heterogeneous nucleation sites. EDS mapping in Figure 6(d, d<sub>1</sub>–d<sub>3</sub>) further demonstrated that these cubic phases were rich in Zr, which was known as Al<sub>3</sub>Zr phase. For AlMgZr-Ti alloy (Figure 7(a, b)), the uniformly distributing  $\alpha$ -Al grains and cubic phases were obvious. EDS mapping in Figure 7(b<sub>3</sub>, b<sub>4</sub>) confirmed that the cubic phases were rich in Ti and Zr. The line scan in Figure 7(c) demonstrated that the atomic ratio of Al:(Zr + Ti) was approximately 3:1, with the atomic ratio of Zr to Ti close to 5:1. Figure 7(c) also indicated that

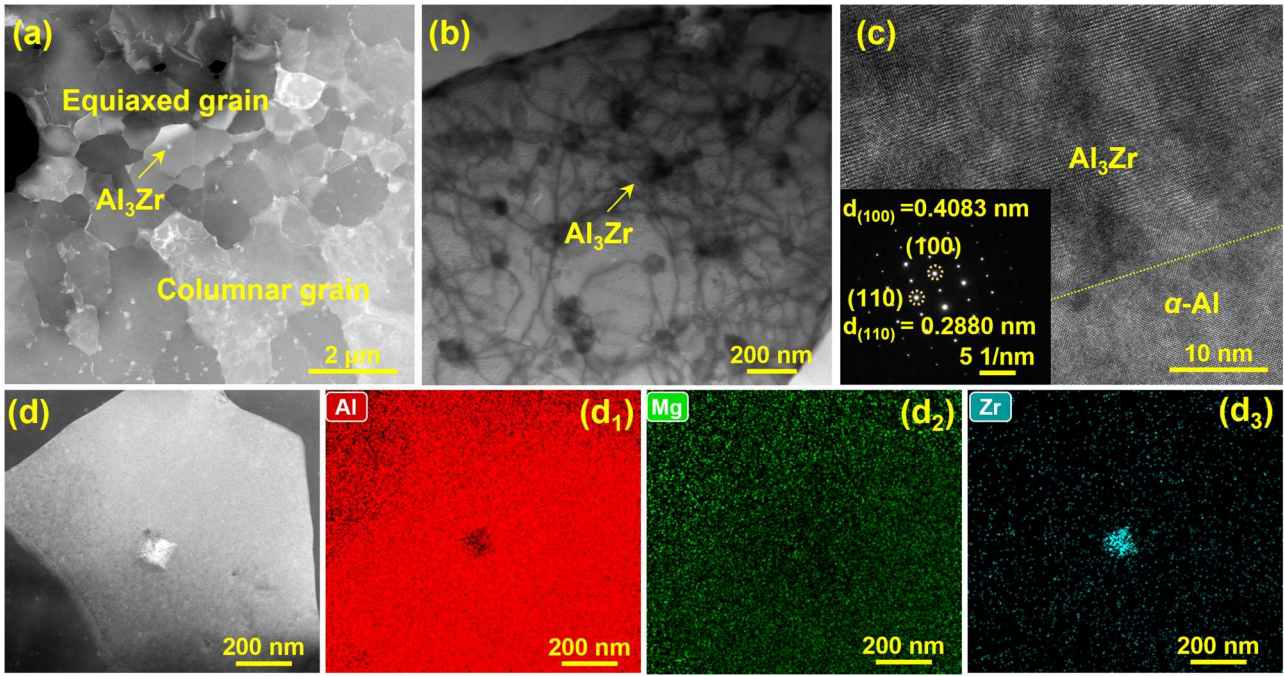


**Figure 6.** TEM images of the as-built AlMgZr alloy. (a) and (b) showing the equiaxed and columnar  $\alpha$ -Al grain, respectively. (c) the HRTEM image of Al<sub>3</sub>Zr and  $\alpha$ -Al. (d) the HAADF micrograph showing a cubic Al<sub>3</sub>Ti phase within  $\alpha$ -Al grain together with the corresponding elemental distribution of Al, Mg, Zr (d<sub>1</sub>-d<sub>3</sub>).

approximately 1/6 of the Ti atoms in the Al<sub>3</sub>Ti-based crystal structure were substituted by Zr atoms. Notably, the fully coherent interface between the  $\alpha$ -Al matrix and Al<sub>3</sub>(Ti, Zr) phase reveals L<sub>12</sub>-ordered structure of the Al<sub>3</sub>(Ti, Zr) phase (Figure 7(d-f)). SAED patterns in Figure 7(h-j) also imply that the Al<sub>3</sub>(Ti, Zr) phase in Figure 7(g) possesses a coherent orientation relationship with the  $\alpha$ -Al matrix:  $[001]_{\text{Al}} // [001]_{\text{Al}_3(\text{Ti}, \text{Zr})}$ ,  $(010)_{\text{Al}} // (010)_{\text{Al}_3(\text{Ti}, \text{Zr})}$ , and  $[011]_{\text{Al}} // [011]_{\text{Al}_3(\text{Ti}, \text{Zr})}$ ,  $(011)_{\text{Al}} // (011)_{\text{Al}_3(\text{Ti}, \text{Zr})}$ , and  $[\bar{1}12]_{\text{Al}} // [\bar{1}12]_{\text{Al}_3(\text{Ti}, \text{Zr})}$ ,  $(1\bar{1}1)_{\text{Al}} // (1\bar{1}1)_{\text{Al}_3(\text{Ti}, \text{Zr})}$ . This investigation revealed the presence of only the L<sub>12</sub>-Al<sub>3</sub>(Ti, Zr) phase in the PBF-LB samples, indicating that the cooling rate (R) within the melt pools was high enough to suppress the formation of DO<sub>22</sub>-Al<sub>3</sub>Ti phase during solidification. Additionally, the element content (at.%) of the  $\alpha$ -Al matrix was determined through EDS map in Figures 6(d) and 7(b), with results summarised in Table 1. A decreased Zr content was observed with Ti addition.

### 3.3. Mechanical properties

Figure 8(a) shows the tensile properties of the as-built (without heat treatment) AlMgZr and AlMgZr-Ti alloys at room temperature. Detailed tensile properties performance statistics was shown in Table 2. Both alloys showed a typical ductile behaviour. The UTS, YS and El of the AlMgZr alloy were 303 , 186 MPa and 21.7%,

respectively. With the additions of Ti, the UTS and YS were 432 and 408 MPa, increased by 42.6% and 119% respectively in comparison with the AlMgZr alloy. The fractured strain reached to 14.7% in the AlMgZr-Ti alloy. From Figure 8(b), the AlMgZr alloy achieves peak strength during ageing in 14 h at 375 °C. An increase of 42.7 HV of hardness and 139 MPa of YS was obtained through ageing at 375 °C for 14 h in AlMgZr alloy, in Figure 8(a, b). Nevertheless, the hardness increase was merely 11.8 HV of hardness and 11 MPa of YS in the AlMgZr-Ti sample, which show minimal age hardening even after extended ageing periods of up to 100 h. This absence of strengthening stands in contrast to the substantial precipitation hardening observed in the AlMgZr alloy. Furthermore, enhanced strength and hardness were achieved in the as-built AlMgZr-Ti alloy compared to both as-built and as-aged AlMgZr alloys. Specifically, it exhibited a hardness of 144.0 HV, an YS of 408 MPa, and an UTS of 432 MPa. Figure 8(c) compares the yield strength vs. elongation of the as-built AlMgZr-Ti alloy with those of other reported Al-Cu, Al-Mg, Al-Si and Al-Zn-Mg-Cu alloys manufactured by PBF-LB [19,31-40]. The as-built AlMgZr-Ti alloy in our work exhibits a good strength-plastic synergy. In Figure 8(d), the columnar grain boundary was clearly observed. In the equiaxed grain zone, dimples were observed in the fracture, as shown in Figure 8(e, f). In Figure 8(g, h), the dimples were also observed in the



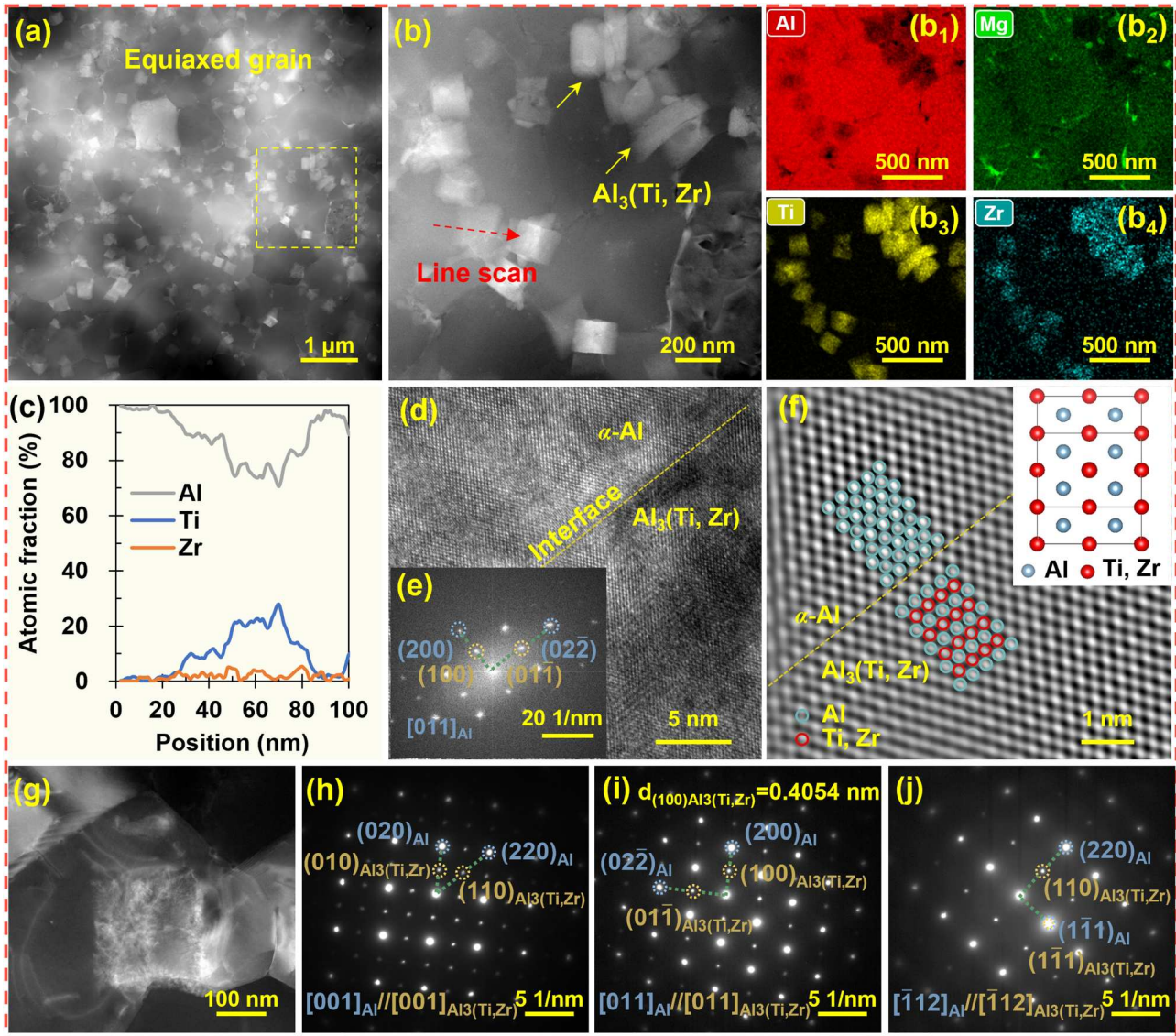


**Figure 7.** TEM images depicting the microstructural characteristics of the as-built AlMgZr-Ti alloy. (a) the  $\alpha$ -Al grain and  $\text{Al}_3(\text{Ti}, \text{Zr})$  phase, (b) the HAADF micrograph together with the corresponding elemental distribution of Al, Mg, Ti, and Zr ( $b_1$ - $b_4$ ). (c) EDS scan along the red line in (b). (d) the HRTEM image of  $\text{Al}_3(\text{Ti}, \text{Zr})$  and  $\alpha$ -Al. (e) the FFT image of (d); (f) the IFFT image of (e). (g)  $\text{Al}_3(\text{Ti}, \text{Zr})$  phase within  $\alpha$ -Al interaction with dislocations; (h-j) the selected area electron diffraction of (g).

**Table 1.** Summary of element content (at.%) of  $\alpha$ -Al matrix in as-built AlMgZr and AlMgZr-Ti alloys.

Alloy	Al	Mg	Zr	Ti
As-built AlMgZr	96.09	3.67	0.24	-
As-built AlMgZr-Ti	95.93	3.75	0.10	0.22

fracture of the as-built AlMgZr-Ti alloy, indicating ductile fracture. In addition, a lot of  $\text{Al}_3(\text{Ti}, \text{Zr})$  precipitates were uniformly distributed within the fractured dimples of the AlMgZr-Ti specimens. In Figure 9(a, b), the UTS at 300 °C increased from 151 MPa to 182 MPa with Ti addition. Clearly, the AlMgZr-Ti alloy delivers good heat resistance, comparable to that of the AlSi10Mg alloy and AlCuCe alloy [41,42].

## 4. Discussion

### 4.1. $\text{Al}_3(\text{Ti}, \text{Zr})$ formation mechanism and precipitation kinetics

From Figure 7, the metastable  $\text{Al}_3(\text{Ti}, \text{Zr})$  phase with the cubic  $L_{12}$  structure was obtained through extremely non-equilibrium solidification up to  $10^7$  K/s. Similar phenomena have been observed in other literatures [43]. Figure 10 shows the  $L_{12}$  structure of  $\text{Al}_3\text{Ti}$ ,  $\text{Al}_3(\text{Ti}, \text{Zr})$  and  $\text{Al}_3\text{Zr}$ . The Zr prefers to replace the 1/6 Zr atom located in the corner of (001) plane. The atomic radius of Zr is approaching both Al and Ti, Zr tend to occupancy in the corner of face-centred cubic structure, as presented in Figure 10(b). The corresponding lattice

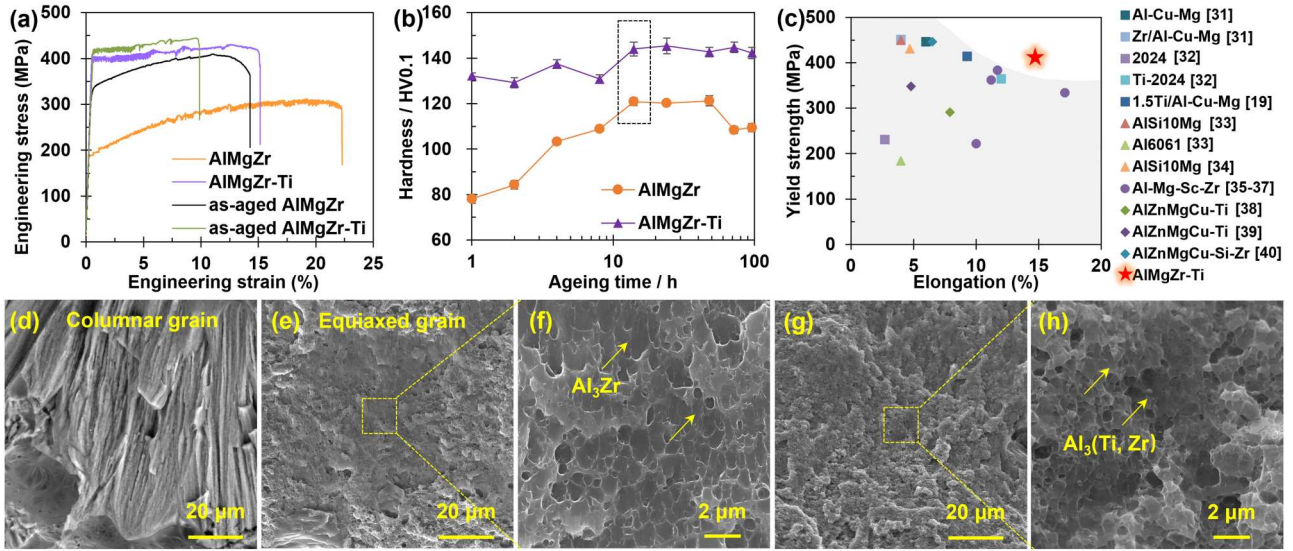


**Figure 8.** (a) Tensile engineering stress-strain curves of the AlMgZr and AlMgZr-Ti alloys at room temperature; (b) the microhardness curves at 375 °C for the AlMgZr and AlMgZr-Ti alloys, the selected area in the box is the peak ageing value. The tensile-stress strain of as-aged AlMgZr and AlMgZr-Ti alloy in (a) was under peak ageing. (c) the yield strength vs. elongation comparison with other published PBF-LB fabricated alloys [19,31-40]. The fractography of as-built (d-f) AlMgZr alloy and (g, h) AlMgZr-Ti alloy.

**Table 2.** Mechanical properties at room temperature for AlMgZr and AlMgZr-Ti alloys.

Sample	YS (MPa)	UTS (MPa)	EI (%)
As-built AlMgZr	186 ± 2	303 ± 6	21.7 ± 1.6
As-built AlMgZr-Ti	408 ± 10	432 ± 13	14.7 ± 3.6
As-aged AlMgZr	325 ± 7	401 ± 15	13.3 ± 2.0
As-aged AlMgZr-Ti	419 ± 3	446 ± 8	11.0 ± 1.7

parameters, lattice misfit, the total energy and the formation enthalpy per atom are shown in Table 3. The calculated energies per atom of bulk Al, Ti and Zr are  $-4.1967\text{ eV}$ ,  $-7.7617\text{ eV}$ ,  $-8.5192\text{ eV}$ , respectively. The substitutionally Zr-occupied Ti phase exhibits stronger atomic bonding compared to the Al<sub>3</sub>Ti phases, as determined by DFT simulations of formation energy per atom. This indicates that the Al<sub>3</sub>(Ti<sub>5/6</sub>, Zr<sub>1/6</sub>) phase is likely to have superior thermal stability relative to the Al<sub>3</sub>Ti phases.

The pronounced age hardening in AlMgZr alloy is attributed to the formation of nanosized, coherent Al<sub>3</sub>Zr (L<sub>12</sub>) precipitates [9,44]. In contrast, no evidence of precipitation strengthening in the AlMgZr-Ti alloy is observed. From Figure 11(a), the initially precipitated phase transformed from Al<sub>3</sub>Zr to Al<sub>3</sub>Ti with Ti addition. The  $f_s$  ending point of primary phase (Al<sub>3</sub>Zr and Al<sub>3</sub>Ti) increased from 0.027 to 0.106, though the ending temperature is basically unchanged, which can deduce that the volume fraction of precipitates increased. In Figure 11(b, c), The mole fraction of Al<sub>3</sub>Ti was 4.55 in the AlMgZr-Ti alloy. The mole fraction of Al<sub>3</sub>Zr were 0.828 and 0.835 in the AlMgZr and AlMgZr-Ti alloys, there is basically no difference in the precipitated Al<sub>3</sub>Zr mole fraction. The Al<sub>3</sub>Ti provides substrate and energy for the precipitation of Al<sub>3</sub>Zr, and the Al<sub>3</sub>(Ti, Zr) formation increased Zr precipitation from  $\alpha$ -Al matrix. In Table 1,

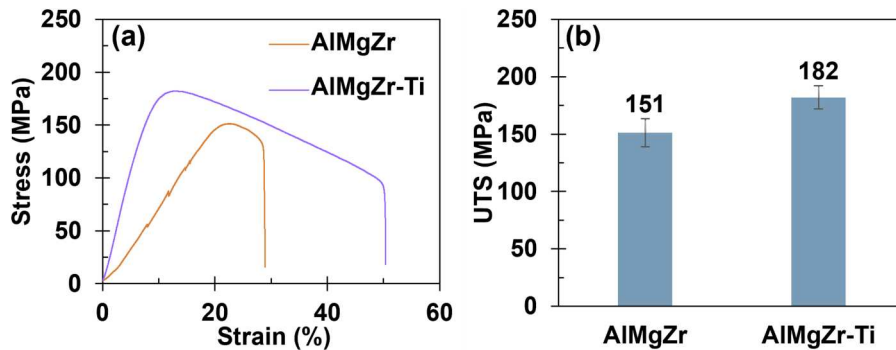


**Figure 9.** Tensile strength of the as-built AlMgZr and AlMgZr-Ti alloys at 300 °C: (a) stress-strain curve; (b) UTS values of as-built AlMgZr and AlMgZr-Ti alloys.



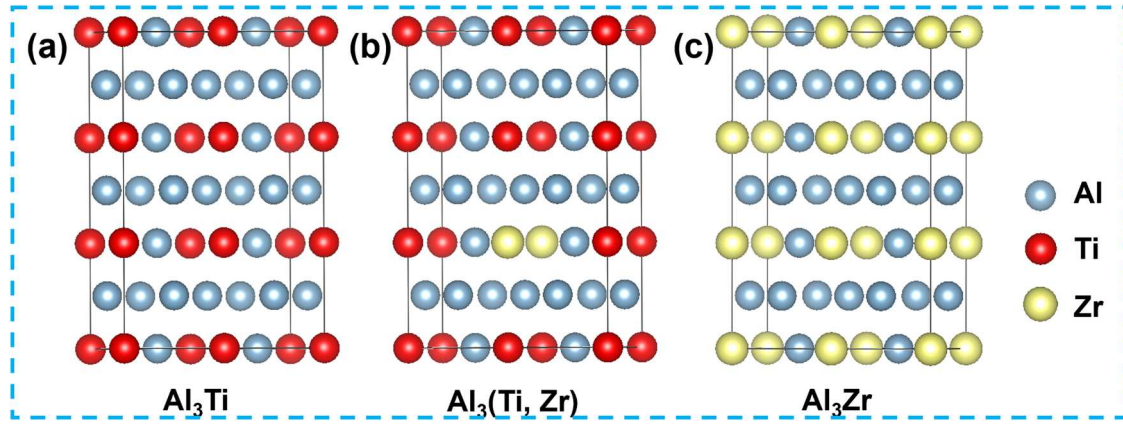


**Figure 10.** The crystal structures of intermetallic,  $L_{12}$  of (a)  $Al_3Ti$ , (b)  $Al_3(Ti, Zr)$ , (c)  $Al_3Zr$ .

**Table 3.** Comparison of lattice parameter, total energy and formation enthalpy of  $L_{12}$  phase in AlMgZr-Ti alloy.

Phase	a / nm	b / nm	c / nm	$E_t$ (eV/atom)	$\Delta H_f$ (eV/atom)
$Al_3Ti$	3.9717	3.9842	3.9729	-5.1201	-0.1286
$Al_3(Ti_{5/6}, Zr_{1/6})$	3.9907	4.0102	3.9932	-5.1644	-0.1794
$Al_3Zr$	4.0969	4.1077	4.0992	-5.4010	-0.4947

a decreased Zr content in the  $\alpha$ -Al matrix was observed with Ti addition, attributed to Zr solute trapping in the  $Al_3(Ti, Zr)$ . Therefore, the lack of age hardening in the AlMgZr-Ti was due to the depletion of Ti/Zr solutes in as-built AlMgZr-Ti alloy.

#### 4.2. Grain refinement and CET

The schematic diagrams of microstructure evolution of AlMgZr and AlMgZr-Ti alloys is shown in Figure 12. The  $Al_3Zr$  was mainly distributed at melt pool boundary as the primary  $Al_3Zr$  particles tend to be formed under a slower solidification interface velocity. During the solidification of AlMgZr-Ti alloy, a substantial fraction of Ti

solutes reacts with aluminum to form a high-density  $L_{12}$ - $Al_3(Ti, Zr)$  phase. This phase exhibits a uniform distribution within the  $\alpha$ -Al matrix and functions as efficient heterogeneous nucleation sites for Al grains [45]. The increased nucleation sites promote grain refinement and CET. In addition, the survival of nuclei is controlled by constitutional supercooling at the solid-liquid (S/L) interface ( $\Delta T_c$ ), which is a key factor impacting the final grain size [46,47]. The initial development rate in the constitutionally undercooled region determines the rate at which adequate undercooling for nucleation is achieved [48]. The growth restriction factor ( $Q$ ) functions as a quantitative indicator to assess a solute's capability to induce  $\Delta T_c$  which is defined as  $Q = \frac{\partial(\Delta T_c)}{\partial(f_s)}$  at  $f_s \rightarrow 0$ , where  $f_s$  is the solid fraction [20]. The  $Q$  value was obtained from Figure 11(a), which was 53.9 K of AlMgZr-Ti and 16.1 K of AlMgZr alloy. The increased  $Q$  might be mainly attributed to the Ti solutes, which can effectively enlarge the overall undercooling and facilitate the nucleation rate, which eventually lead to a

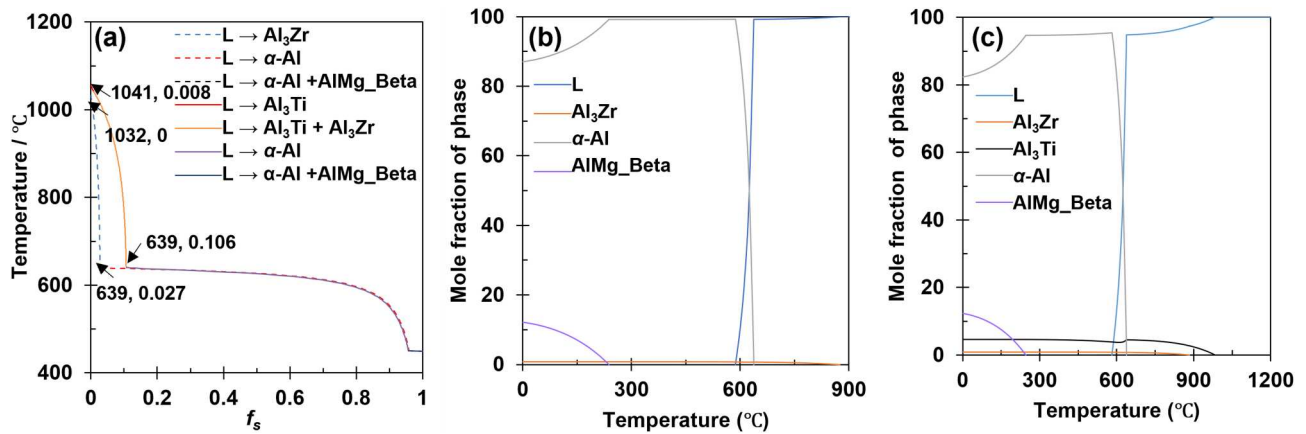


**Figure 11.** (a) The solidification path of the AlMgZr and AlMgZr-Ti alloys. The fraction of phase vary with temperature of (b) the AlMgZr alloy and (c) the AlMgZr-Ti alloy.



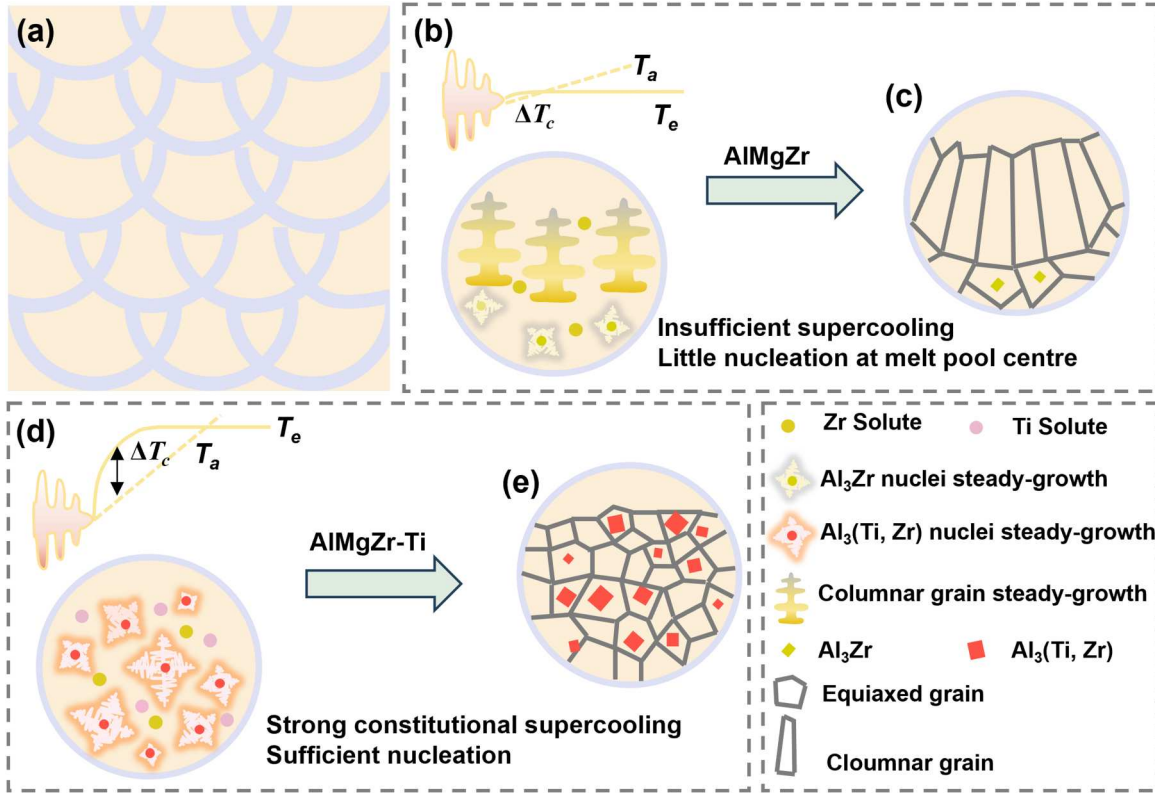


**Figure 12.** Schematic diagrams of microstructure evolution of as-built AlMgZr and AlMgZr-Ti alloys. (a) Melt pool structure; (b, d) the constitutionally undercooled zone and heterogeneous nucleation during initial solidification inside a single melt pool. (c, e) Network structure at the final stage of solidification. Where  $T_a$  represents the equilibrium liquidus temperature, and  $T_e$  stands for the increment in solute content at the interface.

reduction in grain size. Eventually, the dendrites of  $\alpha$ -Al were modified to equiaxed grains by the strong nucleating effect of Al<sub>3</sub>(Ti, Zr) phase with L1<sub>2</sub> structure.

#### 4.3. Processability improvement

In Figure 3(a), the cracks are often found in the intergranular direction parallel to the building direction in AlMgZr alloy, which indicate that the main type of cracks in the AlMgZr alloy is hot cracking [49,50]. Reducing the solidification range and grain size have proven effective to mitigate hot cracking [29]. From Figure 11(a), the solidification interval in both alloy is basically the same. In comparison to the AlMgZr alloy, the improved processability of the AlMgZr-Ti alloy is primarily attributed to grain refinement and the CET of Al grains (Figure 3).

Additionally, previous studies [51,52] has shown the impact of grain refinement on the hot-tearing susceptibility of alloy is closely associated with the strength of the semisolid microstructure. From Figure 3(j-l), a significant decrease in KAM values was observed in the AlMgZr-Ti alloy, indicating enhanced accommodation of thermal stresses during solidification due to increased grain refinement. This was attributed to the equiaxed

grains that can offer a high density of grain boundaries compared to the columnar grains [53]. Furthermore, the presence of finer grains leads to thinner liquid films at the grain boundaries, thereby intensifying the capillary forces at the liquid interface, which is commonly recognised as the critical stress that initiates hot tearing [52]. Studies have shown that fine equiaxed grains elevate the critical stress necessary for hot cracking initiation by increasing the grain boundary density. The critical stress ( $\sigma_c$ ) can be determined using the following approach [38]:

$$\sigma_c = \frac{8\gamma}{\sqrt{3}d} \left( \frac{f_s^M}{1 - f_s^M} \right) \quad (2)$$

where  $\gamma$  represents the liquid surface tension, which is determined to be 0.81 N/m for the AlMgZr and AlMgZr-Ti alloys based on data from the Jmatpro® software. The parameter  $d$  denotes the grain size, defined as the grain width for columnar grains and the average grain size for equiaxed grains.  $M$  is the microstructure parameter, taking values of 1/3 for columnar grains and 1/2 for equiaxed grains [54].  $f_s$  represents the solid fraction. It is clear that ultrafine grains (UFGs)

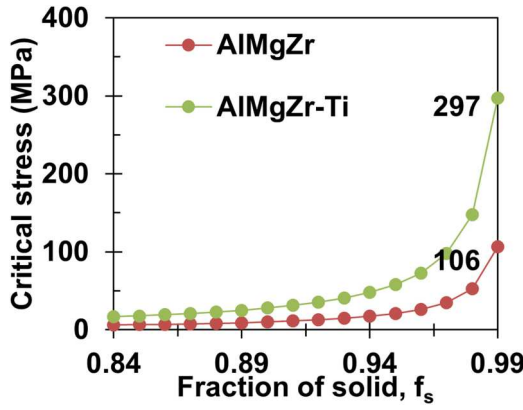


**Figure 13.** The critical hot cracking stress in AlMgZr and AlMgZr-Ti alloys during the terminal solidification stage.

demonstrate a higher critical stress compared to coarse columnar grains (CGs). As the crack normally occurred in columnar grain, the critical stress limit mainly depends on the CGs value within heterogeneous microstructure. Generally, the most vulnerable to cracking always in the terminal solidification stage [49]. Figure 13 depicts the calculated critical stresses of the CGs in AlMgZr and UFGs in AlMgZr-Ti alloys during the final solidification stage, with the  $f_s$  varying from 0.84 to 0.99. With Ti addition, the critical stress is increased from 106 MPa to 297 MPa. Thus, the refined grains in AlMgZr-Ti alloy significantly improved its resistance to hot cracking during PBF-LB process. Additionally, the more tortuous nature of the crack path within this microstructure effectively suppresses crack propagation [19].

Modifying the processing parameters of PBF-LB presents an opportunity to alter the solidification conditions and thermal stress profiles within the melt pools [55]. Through modulating the beam envelope [56], modification the substrate [38] and scanning speed, a reduced solidification velocity may confer a reduction in the cracking susceptibility. With the critical stress increasing threefold, a crack-free AlMgZr-Ti alloy was successfully obtained under different processing parameters. This finding demonstrates that the UFGs in the AlMgZr-Ti alloy can effectively mitigate stresses across a broad spectrum of PBF-LB processing conditions. It is suggested that the elimination of cracking in high-strength Al alloys can be enhanced through the inoculation of the  $\text{Al}_3(\text{Ti}, \text{Zr})$  phase.

#### 4.4. Role of Ti addition in enhancing tensile properties

##### 4.4.1. Strengthening mechanism at room temperature

The overall strengthening mechanisms in the as-built AlMgZr alloy can be attributed to several factors,

including grain boundary strengthening ( $\sigma_{GB}$ ), Orowan strengthening ( $\sigma_{Or}$ ), solid solution strengthening ( $\sigma_{ss}$ ) and dislocation strengthening ( $\sigma_{dis}$ ). With the addition of Ti, the additional strengthening contributions arise from load-bearing strengthening ( $\Delta\sigma_{load}$ ) and thermal expansion mismatch strengthening ( $\sigma_{CTE}$ ) generated by  $\text{Al}_3(\text{Ti}, \text{Zr})$ .

The contribution of grain boundary strengthening was estimated using the Hall-Petch relationship [57]:

$$\sigma_{GB} = \sigma_0 + V_{UFG} k_{HP} d_{UFG}^{-1/2} + V_{CG} k_{HP} d_{CG}^{-1/2} \quad (3)$$

where  $\sigma_0$  represents the friction stress ( $\sigma_0 = 20$  MPa).  $d_{UFG}$  and  $d_{CG}$  were the average grain size of the UFGs and CGs, respectively.  $k_{HP}$  is the Hall-Petch slope, derived from the literature as  $0.14 \text{ MPa/m}^{1/2}$  [17]. For the as-built AlMgZr alloy, approximately 54.3% of the volume fraction consists of UFGs ( $V_{UFG}$ ) with an average size of  $3.1 \mu\text{m}$  was about, leaving 45.7% for columnar grains with an average size of  $12.2 \mu\text{m}$ . In contrast, the as-built AlMgZr-Ti alloy contains 100% UFGs with an average size of  $2.5 \mu\text{m}$ . The calculated  $\sigma_{GB}$  were 81.5 MPa for the as-built AlMgZr alloy and 108.5 MPa for the as-built AlMgZr-Ti alloy.

In both alloys, Mg dissolves in the  $\alpha$ -Al matrix. Due to the mismatch between Mg solute and Al atoms, the dislocation motion was hindered, leading to solid solution strengthening. The solid solution strengthening can be expressed as follows [58]:

$$\sigma_{ss} = 3.1 \varepsilon G c^{1/2} / 700 \quad (4)$$

where  $\varepsilon$  is 0.38 for Mg in Al-Mg alloys.  $G$  represents the shear modulus of  $\alpha$ -Al (25.4 GPa).  $c$  denotes the solute concentration in at.%. In Table 1, the atomic concentrations of Mg in the as-built AlMgZr and AlMgZr-Ti alloys were 3.67 and 3.75 at.%, respectively. The  $\sigma_{ss}$  were calculated as 8.2 MPa for the as-built AlMgZr and 8.3 MPa for the AlMgZr-Ti alloy.

The dislocation strengthening can be determined using Taylor hardening law [59]:

$$\sigma_{dis} = M \alpha G b \quad (5)$$

where  $M$  represents the Taylor factor (3.06).  $a$  denotes a constant for Al alloys (0.27) [60].  $b$  is the Burgers vector for Al (0.286 nm).  $\rho_d$  represents the dislocation density. The dislocation density values were  $2.1 \times 10^{14} \text{ m}^{-2}$  and  $2.4 \times 10^{14} \text{ m}^{-2}$  for the as-built AlMgZr and AlMgZr-Ti alloy. Estimated  $\sigma_{dis}$  were 87.0 MPa for the as-built AlMgZr alloy and 93.0 MPa for the AlMgZr-Ti alloy.

The  $\text{Al}_3\text{Zr}$  and  $\text{Al}_3(\text{Ti}, \text{Zr})$  particles impede dislocation movement, contributing to Orowan strengthening ( $\sigma_{Or}$ ), which can be described by the following equations

[61]:

$$\sigma_{Or} = \frac{0.13Gb}{d_p[(1/2V_p)^{1/3} - 1]} \ln\left(\frac{d_p}{2b}\right) \quad (6)$$

where  $\phi$  is a material constant, taken as 2. The  $\sigma_{Or}$  was estimated to be 11.2 MPa for the AlMgZr alloy and 5.3 MPa for the AlMgZr-Ti alloy.

Additionally, the enhanced tensile strength of AlMgZr-Ti alloy is attributed to the formation of the  $Al_3(Ti, Zr)$  reinforcement phase. During deformation, stress is transferred from the matrix to the  $Al_3(Ti, Zr)$  phase, where  $Al_3(Ti, Zr)$  particles undertake some load and restrict matrix distortion. The direct strengthening effect from  $Al_3(Ti, Zr)$  particles can be attributed to load-bearing strengthening ( $\Delta\sigma_{load}$ ), which can be calculated as below [62,63]:

$$\sigma_{load} = 1.5V_p\sigma_i \quad (7)$$

The bonding strength ( $\sigma_i$ ) between  $Al_3(Ti, Zr)$  and Al matrix is 676 MPa [63]. The  $\sigma_{load}$  attributed to  $Al_3(Ti, Zr)$  particles was estimated to be 139.9 MPa.

The thermal expansion mismatch between  $Al_3(Ti, Zr)$  particles and the  $\alpha$ -Al matrix generates strengthening by blocking of dislocation movement at the  $Al_3(Ti, Zr)$  and  $\alpha$ -Al interfaces. The  $\sigma_{CTE}$  can be calculated as follows [64]:

$$\sigma_{CTE} = 1.25Gb(12\Delta\alpha\Delta TV_p/bd_p(1 - V_p))^{1/2} \quad (8)$$

$\Delta T$  is the difference between the solidification completed temperature (450 °C) and room temperature. The thermal expansion coefficient ( $\Delta\alpha$ ) of the matrix ( $24 \times 10^{-6} K^{-1}$ ) and the  $Al_3Ti$  phase ( $13 \times 10^{-6} K^{-1}$ ) is  $11 \times 10^{-6} K^{-1}$  [65]. The calculated value for  $\Delta\sigma_{CTE}$  in the AlMgZr-Ti alloy was 56.2 MPa.

The total contribution to YS ( $\sigma$ ) contributions from above mechanisms for the AlMgZr and AlMgZr-Ti alloys are summarised in Figure 14(a). Due to the

combined effects of grain boundary strengthening, dislocation strengthening, load-bearing strengthening and thermal expansion mismatch strengthening, the strength of the AlMgZr-Ti alloy was significantly enhanced.

According to Considère criterion (Eq. (9) and Eq. (10)) [8], the strain hardening rate curve for the as-built AlMgZr and AlMgZr-Ti alloys was shown in Figure 14(b).

$$\left(\frac{\partial\sigma}{\partial\varepsilon}\right)_{\dot{\varepsilon}} = \sigma \quad (9)$$

$$\theta = \frac{d\sigma}{d\varepsilon} \quad (10)$$

where  $\sigma$  denotes true stress, and  $\varepsilon$  signifies the true strain.  $\theta$  represents work-hardening rate.

An excellent work hardening behaviour was observed in the AlMgZr alloy, attributed to its bimodal microstructure. The fine equiaxed grains facilitate coordinate deformation, while the coarse grains provide a greater capacity for dislocation accommodation. Such heterogeneous structures effectively alleviate stress concentrations and promote strain delocalisation, thereby enhancing strain hardening ability and improving ductility [66,67]. Consequently, the AlMgZr alloy exhibits excellent ductility. With Ti addition, grain refinement occurred, which was beneficial for increasing elongation. However, the reduction in the work-hardening rate was not conducive to maintaining ductility. Moreover, the increased volume fraction and average size of  $Al_3(Ti, Zr)$  phase can lead to stress concentration during deformation and serve as crack nucleation sites. Nevertheless, the  $Al_3(Ti, Zr)$  phase maintains an  $L1_2$  structure with low lattice mismatch, which is advantageous for elongation [68,69]. Due to the combined effects of these factors, although the elongation slightly decreased with Ti addition, the AlMgZr-Ti alloy still maintained good ductility.

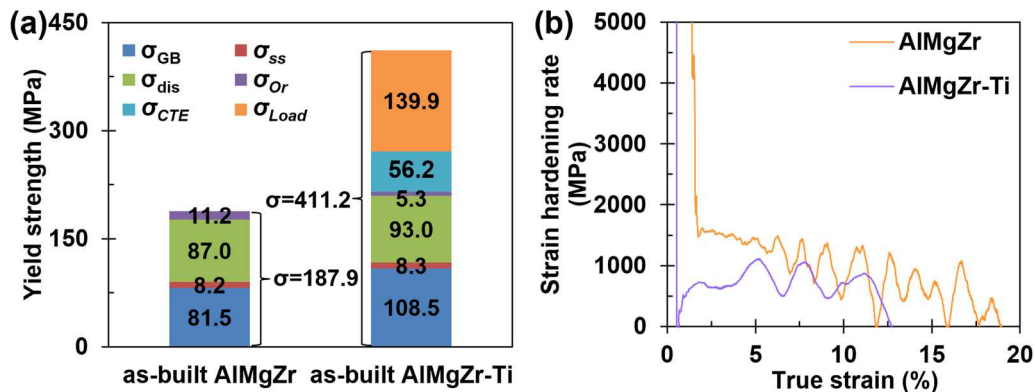


**Figure 14.** (a) Summary of the various strengthening contributions to the yield strength in the as-built AlMgZr and the as-built AlMgZr-Ti alloy. (b) the strain hardening rate curve of as-built AlMgZr and AlMgZr-Ti alloys.



#### 4.4.2. The evaluate of AlMgZr-Ti alloy at elevated temperature

In Figure 9(b), the hardness of both alloys increased after ageing at 375 °C for 100 h, demonstrating high thermal stability in both alloys. Specifically, the hardness of the AlMgZr-Ti alloy after ageing at 375 °C for 100 h was higher than that of the AlMgZr alloy. Additionally, an increase of 31 MPa in UTS at 300 °C was observed in the AlMgZr-Ti alloy compared to the AlMgZr alloy. Given the low solubility and diffusivity of Zr (0.083 at.%,  $1.20 \times 10^{-20}$  m<sup>2</sup>/s at 400 °C), and the low lattice parameter mismatch between the Al<sub>3</sub>Zr phase and the  $\alpha$ -Al matrix, the Al<sub>3</sub>Zr phase was recognised as thermally stable phase [70,71]. Compared to Zr, the diffusion coefficient of Ti in solid Al ( $7.39 \times 10^{-22}$  m<sup>2</sup>/s at 400 °C) is lower, resulting in improved coarsening resistance of the Al<sub>3</sub>(Ti, Zr) phase compared to Al<sub>3</sub>Zr phase [72]. Moreover, the L1<sub>2</sub>-structured Al<sub>3</sub>(Ti, Zr) phase exhibits full coherence with the  $\alpha$ -Al matrix, leading to a lower interfacial energy and contributing to high temperature stability [73]. Notably, the high volume fraction (6.9%) of submicron Al<sub>3</sub>(Ti, Zr) phase effectively stabilises grain boundaries and pins dislocations at elevated temperature, which are the primary strengthening mechanisms of the AlMgZr-Ti alloy at elevated temperature. Although grain refinement may not be conducive to high temperature performance, the introduction of a high volume fraction of thermally stable Al<sub>3</sub>(Ti, Zr) phase resulted in improved tensile strength at 300 °C. This finding provides new insights into the development of high temperature resistant aluminum alloy for additive manufacturing.

## 5. Conclusions

- (1) The addition of Ti accelerated the precipitation of Zr from  $\alpha$ -Al, meanwhile the Al<sub>3</sub>(Ti, Zr) particles with high volume fraction were formed during the solidification process in PBF-LB. The L1<sub>2</sub>-Al<sub>3</sub>(Ti, Zr) promoted the grain refinement and CET. Moreover, the presence of excess Ti solutes promoted the refinement of  $\alpha$ -Al grains by increasing constitutional supercooling.
- (2) Compared to the CGs in the AlMgZr alloy, the UFGs of the AlMgZr-Ti alloy exhibits enhanced hot-tearing resistance. Consequently, a crack-free AlMgZr-Ti alloy was successfully produced using PBF-LB processing.
- (3) In comparison to the AlMgZr alloy, the yield strength and ultimate tensile strength of AlMgZr-Ti alloy increased significantly, rising from 186 and 303

MPa to 408 and 432 MPa, respectively. This improvement in yield strength was primarily attributed to grain boundary strengthening, the dislocations strengthening, load-bearing strengthening provided by Al<sub>3</sub>(Ti, Zr) particles and thermal expansion mismatch strengthening.

- (4) The AlMgZr-Ti alloy is heat resistant at elevated temperature due to the high thermal stability Al<sub>3</sub>(Ti, Zr) phase pinning the grain boundaries. At 300 °C, the ultimate tensile strength of the AlMgZr-Ti alloy was measured at 182 MPa.

## Credit authorship contribution statement

**Mengzhen Zhu** (First author): Data curation, Writing – original draft, Investigation; **Jianying Wang**: Investigation, Writing – review & editing; **Tao Wen**: Methodology, Writing – review & editing, Supervision; **Zhongxue He**: Investigation; **Xixi Dong**: Conceptualisation, Writing – review & editing; **Dong Qiu**: Conceptualisation, Writing – review & editing; **Shouxun Ji**: Validation, Writing – review & editing; **Yun Wang**: Writing – review & editing; **Hailin Yang**: Conceptualisation, Funding acquisition, Project administration, Writing – review & editing, Supervision.

## Disclosure statement

No potential conflict of interest was reported by the author(s).

## Funding

This work was supported by the National Natural Science Foundation of China under [grant number 52071343] and the Central South University Postgraduate Research and Innovation Project, China under [Grant 2024ZZTS0079].

## Data availability statement

Data are available from the corresponding author on reasonable request.

## References

- [1] Wang JY, Yang HL, Liu ZL, et al. Compositional regulation in additive manufacturing of precipitation-hardening (CoCrNi)<sub>94</sub>Ti<sub>3</sub>Al<sub>3</sub> medium-entropy superalloy: cellular structure stabilization and strength enhancement. *Compos Part B-Eng*. 2024;281:111570.
- [2] Wang ZN, Lin X, Wang LL, et al. Microstructure evolution and mechanical properties of the wire + arc additive manufacturing Al-Cu alloy. *Addit Manuf*. 2021;47:102298.
- [3] Blakey-Milner B, Gradl P, Snedden G, et al. Metal additive manufacturing in aerospace: a review. *Mater Des*. 2021;209:110008.

- [4] Aboulkhair NT, Simonelli M, Parry L, et al. 3D printing of aluminium alloys: additive manufacturing of aluminium alloys using selective laser melting. *Prog Mater Sci.* [2019](#);106:100578.
- [5] Opprecht M, Garandet JP, Roux G, et al. A solution to the hot cracking problem for aluminium alloys manufactured by laser beam melting. *Acta Mater.* [2020](#);197:40–53.
- [6] Rometsch PA, Zhu YM, Wu XH, et al. Review of high-strength aluminium alloys for additive manufacturing by laser powder bed fusion. *Mater Des.* [2022](#);219:110779.
- [7] Wen T, Li ZC, Wang JY, et al. CALPHAD aided design of a crack-free Al-Mg-Si-Ti alloy with high strength: heterogeneous nucleation and eutectic filling during additive manufacturing. *Virtual Phys Prototyp.* [2024](#);19(1):2378930.
- [8] Wang JY, Gao JB, Yang HL, et al. High-strength Al-5Mg<sub>2</sub>Si-2Mg-2Fe alloy with extremely high Fe content for green industrial application through additive manufacturing. *Virtual Phys Prototyp.* [2023](#);18(1):2235587.
- [9] Zhu MZ, Zhang MZ, Wang JY, et al. Microstructural evolution and strength enhancement in laser powder bed fusion Al-Mg-Yb-Zr alloys. *J Alloys Compd.* [2024](#);1008:176564.
- [10] Zhou L, Hyer H, Park S, et al. Microstructure and mechanical properties of Zr-modified aluminum alloy 5083 manufactured by laser powder bed fusion. *Addit Manuf.* [2019](#);28:485–496.
- [11] Croteau JR, Griffiths S, Rossell MD, et al. Microstructure and mechanical properties of Al-Mg-Zr alloys processed by selective laser melting. *Acta Mater.* [2018](#);153:35–44.
- [12] Xu R, Li RD, Yuan TC, et al. Laser powder bed fusion of Al-Mg-Zr alloy: microstructure, mechanical properties and dynamic precipitation. *Mater Sci Eng A.* [2022](#);859:144181.
- [13] Luo YH, Pan QL, Sun YQ, et al. Hardening behavior of Al-0.25Sc and Al-0.25Sc-0.12Zr alloys during isothermal annealing. *J Alloys Compd.* [2020](#);818:152922.
- [14] Belevi F, Casati R, Andrianopoli C, et al. Investigation and characterization of an Al-Mg-Zr-Sc alloy with reduced Sc content for laser powder bed fusion. *J Alloys Compd.* [2022](#);924:166519.
- [15] Li G, Ruan G, Huang YH, et al. Facile and cost-effective approach to additively manufacture crack-free 7075 aluminum alloy by laser powder bed fusion. *J Alloys Compd.* [2022](#);928:167097.
- [16] Zhang TL, Huang ZH, Yang T, et al. In situ design of advanced titanium alloy with concentration modulations by additive manufacturing. *Science.* [2021](#);374(6566):478–482.
- [17] Li RD, Wang MB, Li ZM, et al. Developing a high-strength Al-Mg-Si-Sc-Zr alloy for selective laser melting: crack-inhibiting and multiple strengthening mechanisms. *Acta Mater.* [2020](#);193:83–98.
- [18] Martin JH, Yahata BD, Hundley JM, et al. 3D printing of high-strength aluminium alloys. *Nature.* [2017](#);549(7672):365–369.
- [19] Tan QY, Zhang JQ, Sun Q, et al. Inoculation treatment of an additively manufactured 2024 aluminium alloy with titanium nanoparticles. *Acta Mater.* [2020](#);196:1–16.
- [20] Jiang FQ, Tang L, Ye HQ, et al. The role of TiH<sub>2</sub> on microstructure and mechanical properties of Al-Zn-Mg-Cu alloy fabricated by laser powder bed fusion. *Mater Sci Eng A.* [2023](#);869:144819.
- [21] Wang TR, Zeng W, Xia T, et al. Suppressing formation of microcracks in laser powder bed fusion manufactured AA6061 aluminum alloy by introducing mechanical alloyed Al-25at%Ti particles. *Mater Lett.* [2024](#);367:136568.
- [22] Wang Q, Guo YM, Li FF, et al. Microstructures and mechanical properties of nano-TiC/Ti-refined Al-Mg alloys prepared by wire arc additive manufacturing. *Mater Charact.* [2024](#);208:113614.
- [23] Perdew JP, Burke K, Ernzerhof M. Generalized gradient approximation made simple. *Phys Rev Lett.* [1996](#);77(18):3865–3868.
- [24] Kim K, Zhou BC, Wolverton C. First-principles study of crystal structure and stability of T1 precipitates in Al-Li-Cu alloys. *Acta Mater.* [2018](#);145:337–346.
- [25] Simchi A. Direct laser sintering of metal powders: mechanism, kinetics and microstructural features. *Mater Sci Eng A.* [2006](#);428(1-2):148–158.
- [26] Bi J, Wu LK, Liu ZQ, et al. Microstructure, mechanical properties and multiphase synergistic strengthening mechanisms of a novel laser additive manufactured AlNi6TiZr alloy. *J Mater Sci Technol.* [2024](#);178:59–69.
- [27] Zhang H, Zhu HH, Qi T, et al. Selective laser melting of high strength Al-Cu-Mg alloys: processing, microstructure and mechanical properties. *Mater Sci Eng A.* [2016](#);656:47–54.
- [28] Tan QY, Liu YG, Fan ZQ, et al. Effect of processing parameters on the densification of an additively manufactured 2024 Al alloy. *J Mater Sci Technol.* [2020](#);58:34–45.
- [29] Wen T, Li ZC, Wang JY, et al. From crack-prone to crack-free: eliminating cracks in additively manufacturing of high-strength Mg<sub>2</sub>Si-modified Al-Mg-Si alloys. *J Mater Sci Technol.* [2025](#);204:276–291.
- [30] Nayak SS, Pabi SK, Murty BS. High strength nanocrystalline L1<sub>2</sub>-Al<sub>3</sub>(Ti,Zr) intermetallic synthesized by mechanical alloying. *Intermetallics.* [2007](#);15(1):26–33.
- [31] Zhang H, Zhu HH, Nie XJ, et al. Effect of Zirconium addition on crack, microstructure and mechanical behavior of selective laser melted Al-Cu-Mg alloy. *Scr Mater.* [2017](#);134:6–10.
- [32] Tan QY, Zhang JQ, Sun Q, et al. Inoculation treatment of an additively manufactured 2024 aluminium alloy with titanium nanoparticles. *Acta Mater.* [2020](#);196:1–16.
- [33] Maamoun AH, Xue YF, Elbestawi MA, et al. The effect of selective laser melting process parameters on the microstructure and mechanical properties of Al6061 and AlSi10Mg alloys. *Materials (Basel).* [2019](#);12(1):12–35.
- [34] Xiao YK, Chen H, Bian ZY, et al. Enhancing strength and ductility of AlSi10Mg fabricated by selective laser melting by TiB<sub>2</sub> nanoparticles. *J Mater Sci Technol.* [2022](#);109:254–266.
- [35] Zhao JR, Lee LY, Chang KC, et al. A novel two-stage heat treatment with medium-temperature aging influence on microstructure, Al<sub>3</sub>(Sc, Zr) nanoprecipitation, and application properties, enhancing selective laser melting of Al-Mg-Sc-Zr alloy. *Nanomaterials.* [2022](#);12(12):2078.
- [36] Li RD, Chen H, Zhu HB, et al. Effect of aging treatment on the microstructure and mechanical properties of Al-3.02Mg-0.2Sc-0.1Zr alloy printed by selective laser melting. *Mater Des.* [2019](#);168:107668.
- [37] Ma RL, Peng CQ, Cai ZY, et al. Effect of bimodal microstructure on the tensile properties of selective laser melt Al-Mg-Sc-Zr alloy. *J Alloys Compd.* [2020](#);815:152422.

- [38] Tan QY, Fan ZQ, Tang XQ, et al. A novel strategy to additively manufacture 7075 aluminium alloy with selective laser melting. *Mater Sci Eng A*. **2021**;821:141638.
- [39] Jiang FQ, Tang L, Ye HQ, et al. The role of TiH<sub>2</sub> on microstructure and mechanical properties of Al-Zn-Mg-Cu alloy fabricated by laser powder bed fusion. *Mater Sci Eng A*. **2023**;869:144819.
- [40] Li LB, Li RD, Yuan TC, et al. Microstructures and tensile properties of a selective laser melted Al-Zn-Mg-Cu (Al7075) alloy by Si and Zr microalloying. *Mater Sci Eng A*. **2020**;787:139492.
- [41] Perez-Prado MT, Martin A, Shi D, et al. An Al-5Fe-6Cr alloy with outstanding high temperature mechanical behavior by laser powder bed fusion. *Addit Manuf*. **2022**;55:102828.
- [42] Bahl S, Plotkowski A, Sisco K, et al. Elevated temperature ductility dip in an additively manufactured Al-Cu-Ce alloy. *Acta Mater*. **2021**;220:117285.
- [43] Málek P, Janeček M, Smola B, et al. Structure and properties of rapidly solidified Al-Zr-Ti alloys. *J Mater Sci*. **2000**;35(10):2625–2633.
- [44] Knipling KE, Dunand DC, Seidman DN. Nucleation and precipitation strengthening in dilute Al-Ti and Al-Zr alloys. *Metall Mater Trans A*. **2007**;38(10):2552–2563.
- [45] Li JH, Xiang ZL, Shen GL, et al. Microstructure evolution and strengthening mechanisms of cast Al-Cu-Mn alloy via Ti-Zr-synergistic micro-alloying. *Int J Metalcast*. **2024**;18(4):3190–3209.
- [46] StJohn DH, Qian M, Easton MA, et al. The interdependence theory: the relationship between grain formation and nucleant selection. *Acta Mater*. **2011**;59(12):4907–4921.
- [47] Quedate TE, Dinsdale AT, Greer AL. Thermodynamic modelling of growth-restriction effects in aluminium alloys. *Acta Mater*. **2005**;53(5):1323–1334.
- [48] Easton MA, StJohn DH. A model of grain refinement incorporating alloy constitution and potency of heterogeneous nucleant particles. *Acta Mater*. **2001**;49(10):1867–1878.
- [49] Kou S. A criterion for cracking during solidification. *Acta Mater*. **2015**;88:366–374.
- [50] Fu J, Li H, Song X, et al. Multi-scale defects in powder-based additively manufactured metals and alloys. *J Mater Sci Technol*. **2022**;122:165–199.
- [51] Eskin DG, Katgerman L. Mechanical properties in the semi-solid state and hot tearing of aluminium alloys. *Prog Mater Sci*. **2004**;49(5):629–711.
- [52] Tang Z, Vollertsen F. Influence of grain refinement on hot cracking in laser welding of aluminum. *Weld World*. **2014**;58(3):355–366.
- [53] Spittle JA, Cushway AA. Influences of superheat and grain structure on hot-tearing susceptibilities of Al-Cu alloy castings. *Metals Technol*. **1983**;10B(1):6–13.
- [54] Lahaie DJ, Bouchard M. Physical modeling of the deformation mechanisms of semisolid bodies and a mechanical criterion for hot tearing. *Metall Mater Trans B*. **2001**;32(4):697–705.
- [55] DebRoy T, Wei HL, Zuback JS, et al. Additive manufacturing of metallic components – process, structure and properties. *Prog Mater Sci*. **2018**;92:112–224.
- [56] Chen YH, Zhang DY, O Toole P, et al. In situ observation and reduction of hot-cracks in laser additive manufacturing. *Commun Mater*. **2024**;5(1):84–93.
- [57] Zhu ZG, Ng FL, Seet HL. Superior mechanical properties of a selective-laser-melted AlZnMgCuScZr alloy enabled by a tunable hierarchical microstructure and dual-nanoprecipitation. *Mater Today*. **2022**;52:90–101.
- [58] Kendig KL, Miracle DB. Strengthening mechanisms of an Al-Mg-Sc-Zr alloy. *Acta Mater*. **2002**;50(16):4165–4175.
- [59] Buttard M, Freixes ML, Josserond C, et al. Ageing response and strengthening mechanisms in a new Al-Mn-Ni-Cu-Zr alloy designed for laser powder bed fusion. *Acta Mater*. **2023**;259:119271.
- [60] Deschamps A, Brechet Y. Influence of predeformation and ageing of an Al-Zn-Mg alloy—II. Modeling of precipitation kinetics and yield stress. *Acta Mater*. **1998**;47(1):293–305.
- [61] Zhang Z, Chen DL. Consideration of Orowan strengthening effect in particulate-reinforced metal matrix nanocomposites: a model for predicting their yield strength. *Scr Mater*. **2006**;54(7):1321–1326.
- [62] Nardone VC, Prew KM. On the strength of discontinuous silicon carbide reinforced aluminum composites. *Scr Metall*. **1986**;20(1):43–48.
- [63] Li XP, Ji G, Chen Z, et al. Selective laser melting of nano-TiB<sub>2</sub> decorated AlSi10Mg alloy with high fracture strength and ductility. *Acta Mater*. **2017**;129:183–193.
- [64] Liu ZW, Cheng N, Zheng QL, et al. Processing and tensile properties of A356 composites containing in situ small-sized Al<sub>3</sub>Ti particulates. *Mater Sci Eng A*. **2018**;710:392–399.
- [65] Ma Y, Mei QS, Li CL, et al. Microstructure and mechanical behavior of Al-TiAl<sub>3</sub> composites containing high content uniform dispersion of TiAl<sub>3</sub> particles. *Mater Sci Eng A*. **2020**;786:139435.
- [66] Tang YB, Liu CZ, Liu J, et al. Improving the ductility of Al matrix composites through bimodal structures: precise manipulation and mechanical responses to coarse grain fraction. *Mater Sci Eng A*. **2023**;875:145139.
- [67] Wu H, Fan GH. An overview of tailoring strain delocalization for strength-ductility synergy. *Prog Mater Sci*. **2020**;113:100675.
- [68] Abdellahi M, Jabbarzare S, Ghayour H, et al. Thermal and X-ray analyses of aluminum-titanium nanocomposite powder. *J Therm Anal Calorim*. **2018**;131(2):853–863.
- [69] Ghosh G, Vaynman S, Asta M, et al. Stability and elastic properties of L1<sub>2</sub>-(Al,Cu)<sub>3</sub>(Ti,Zr) phases: Ab initio calculations and experiments. *Intermetallics*. **2007**;15(1):44–54.
- [70] Knipling KE, Dunand DC, Seidman DN. Precipitation evolution in Al-Zr and Al-Zr-Ti alloys during aging at 450–600 °C. *Acta Mater*. **2008**;56(6):1182–1195.
- [71] Knipling KE, Dunand DC, Seidman DN. Criteria for developing castable, creep-resistant aluminum-based alloys – a review. *Z Metallkd*. **2006**;97(3):246–265.
- [72] Knipling KE, Dunand DC, Seidman DN. Precipitation evolution in Al-Zr and Al-Zr-Ti alloys during isothermal aging at 375–425 °C. *Acta Mater*. **2008**;56(1):114–127.
- [73] Tsau CH, Chen YC. The coarsening of the precipitates in melt-spun Al – Ti – Zr ribbons. *Mater Chem Phys*. **2002**;73(2):111–117.